On Establishing Buckling Knockdowns for Imperfection-Sensitive Shell Structures

S. Gerasimidis
Civil and Environmental Engineering Department,
University of Massachusetts,
Amherst, MA 01003

E. Virot
Emergent Complexity in Physical Systems Laboratory,
Ecole Polytechnique Federale de Lausanne,
Lausanne CH 1015, Switzerland;
School of Engineering and Applied Sciences,
Harvard University,
Cambridge, MA 02138

J. W. Hutchinson
School of Engineering and Applied Sciences,
Harvard University,
Cambridge, MA 02138

S. M. Rubinstein
School of Engineering and Applied Sciences,
Harvard University,
Cambridge, MA 02138

This paper investigates issues that have arisen in recent efforts to revise long-standing knockdown factors for elastic shell buckling, which are widely regarded as being overly conservative for well-constructed shells. In particular, this paper focuses on cylindrical shells under axial compression with emphasis on the role of local geometric dimple imperfections and the use of lateral force probes as surrogate imperfections. Local and global buckling loads are identified and related for the two kinds of imperfections. Buckling loads are computed for four sets of relevant boundary conditions revealing a strong dependence of the global buckling load on overall end-rotation constraint when local buckling precedes global buckling. A reasonably complete picture emerges, which should be useful for informing decisions on establishing knockdown factors. Experiments are performed using a lateral probe to study the stability landscape for a cylindrical shell with overall end rotation constrained in the first set of tests and then unconstrained in the second set of tests. The nonlinear buckling behavior of spherical shells under external pressure is also examined for both types of imperfections. The buckling behavior of spherical shells is different in a number of important respects from that of the cylindrical shells, particularly regarding the interplay between local and global buckling and the post-buckling load-carrying capacity. These behavioral differences have bearing on efforts to revise buckling design rules. The present study raises questions about the perspicacity of using probe force imperfections as surrogates for geometric dimple imperfections. [DOI: 10.1115/1.4040455]

Keywords: shell buckling, knockdown factors, minimum buckling loads, cylindrical shells, spherical shells, dimple imperfections

1 Introduction

Design rules for buckling of highly imperfection-sensitive structures like cylindrical shells under axial compression and spherical shells under external pressure emerged in the 1950s and 1960s driven by the development of light weight shell structures for space and aeronautics and for many other structural applications as well. Due to the large scatter observed in test data and the difficulty of measuring imperfections and computing their degrading effects, the rules which emerged in the 1960s were heavily based on test data and expressed in the form of conservative empirical formulas. The rich history of shell buckling is the topic of the book by Elishakoff [1], which provides a rather complete background to the underlying technical issues addressed in this paper. The most well-known example of the design formulas which emerged five decades ago is the NASA formula [2] for elastic buckling of cylindrical shells under axial compression. It expresses the axial design load at buckling, F, in terms of the axial buckling load of the perfect shell, the so-called classical buckling load, F_C, as $F = \kappa F_C$, where the knockdown factor κ depends on the shell radius to thickness ratio, R/t, according to

$$\kappa = 1 - 0.901\left(1 - e^{-\frac{1}{16}\sqrt{\frac{R}{t}}}\right) \tag{1}$$

This formula reflects the fact that typical thin shells may buckle at loads as low as 50% to below 20% of their perfect counterpart depending on R/t. A low knockdown factor, $\kappa \approx 0.20$, has generally also been adopted for the elastic buckling of spherical shells subject to external pressure because the data base for spherical shells was smaller and the behavior was believed to be similar.

Five decades after these rules were put in place they are now in the process of being revised in recognition of the widely held view that the knockdown factors are overly conservative for most well-constructed shells. Concomitantly, extraordinary advances have occurred in the intervening years in both computation methods for buckling and in experimental techniques to measure imperfections and to test and fabricate shells. Widely available commercial computational codes are capable of accurately evaluating the buckling load of a shell if its imperfections are correctly incorporated into the computational model. The efforts to update the design rules for shell buckling are worldwide, with computational and experimental work toward these goals underway in Europe [3–8], the U.S. [9–11] and China [12,13]. Early work initiated in the former Soviet Union has also been influential in the recent efforts some of which is cited in Refs. [7] and [14]. Because of its structural importance and its canonical role as one of the most imperfection-sensitive structure/loading combinations, much of the basic work is centered on the elastic buckling of cylindrical shells under axial compression.

This paper focuses on new developments that have emerged in the recent literature noted above, first for elastic buckling of cylindrical shells under axial compression and then for spherical shells under external pressure. Recent efforts to arrive at less conservative knockdown factors are premised on the notion that many of the shells comprising the experimental data base assembled in the 1960s and 1970s were not manufactured to the standards possible today. They are also based on the notion that most of the theoretical and numerical imperfection-sensitivity studies conducted in those early years assumed geometric imperfections that were not realistic leading to overly large buckling reductions. Shapes in the form of the classical buckling mode itself, for which Koiter's theory [15,16] predicts the most dramatic load reductions, are considered to be unrealistic in most instances. The new efforts also recognize that detailed historical knowledge of shell

Contributed by the Applied Mechanics Division of ASME for publication in the Journal of Applied Mechanics. Manuscript received May 22, 2018; final manuscript received May 26, 2018; published online June 18, 2018. Editor: Yonggang Huang.

imperfections, such as that cataloged by Árbocz [17], is important for providing general insights into representative imperfections. However, cataloged imperfections are not likely to be directly useful for establishing the buckling load of a newly designed shell that has not yet been manufactured. It has also been recognized that localized dimple-like imperfections are almost certainly more representative of realistic imperfections than highly correlated imperfection patterns spread over the entire shell which tend to produce the largest knockdowns in buckling. With the exception of an early study by Berry and Rotter [18] and a comprehensive study in the 2006 Ph.D. thesis of Wullschleger [19], which will be discussed in this paper, there appears to be little published work employing modern computational methods to investigate the role of localized geometric dimple imperfections on the buckling of cylindrical shells in axial compression.

One recent approach makes use of a lateral probing force as a surrogate imperfection intended to represent realistic local geometric dimple-like imperfections and computes the buckling behavior as a function of imperfection amplitude. Other work [18,19], including that in the present paper, studies the effect of geometric dimple imperfections themselves on the buckling behavior. For cylindrical shells under axial compression with either a geometric dimple imperfection or a probing force imperfection, the recent work has revealed the existence of two buckling thresholds: an axial load at which local buckling occurs and a higher load at which catastrophic global buckling takes place. Moreover, in the imperfection range in which the two thresholds exist, the global buckling load is nearly independent of the imperfection amplitude such that a minimum load for global buckling can be identified. There may be some applications for which local buckling of the shell can be tolerated, in which case the minimum global buckling load might be used to establish the knockdown factor. We will not adopt this view in the present study. Here, we will seek a clear understanding of the relation of both local and global buckling to the shell's imperfection and loading end conditions. We will regard the first buckling load encountered as *the* buckling load. If local buckling happens to precede global buckling then the gap between the two loads can be regarded as a "safety cushion." Finally, for both cylindrical shells under axial compression and spherical shells under external pressure, we critically examine whether probing force imperfections can be employed effectively as surrogates for geometric dimple imperfections.

In brief, Sec. 2 focuses on cylindrical shells under axial compression with probing force imperfections. We reproduce some earlier results and show that the load for global buckling of otherwise fully clamped shells depends strongly on whether overall rotation at the ends is allowed or suppressed. Four sets of clamped boundary conditions are considered involving the two limits of prescribed end shortening and prescribed axial load, in each case with overall end rotation allowed or suppressed. In Sec. 3, experiments are reported, which demonstrate this difference between probing a clamped shell tested under prescribed end shortening with no overall end rotation and the same shell tested with end rotation allowed. In Sec. 4, for the same suite of boundary conditions considered for the probing force imperfection, we study the buckling behavior of the cylindrical shells with local geometric dimple imperfections, characterizing both local and global buckling behavior. Comparison with the behavior for the shells with the probing force imperfections gives clear insight as to whether one type of imperfection can indeed be the surrogate for the other. In Sec. 5, we contrast the buckling behavior of spherical shells under external pressure with that of cylindrical shells under axial compression. In particular, it is shown that the nonlinear buckling behavior of the two types of shells is qualitatively different in several important respects and the protocol for assigning knockdown factors to one may not apply to the other. Conclusions and recommendations are given in Sec. 6.

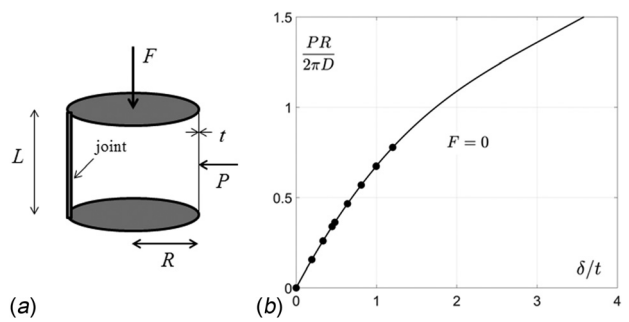

Fig. 1 (*a*) Geometry and conventions for a lateral probe force imperfection. (*b*) Dimensionless relation between the probing force, *P*, and the inward radial deflection at the probe, δ, with no end shortening for case A. The values of *P* chosen for the simulations of Haynie et al. [10] are denoted by solid dots on the curve.

2 The Influence of End Conditions on the Elastic Buckling Behavior of Cylindrical Shells Under Axial Compression With Probing Force Imperfections

We begin by replicating the computational results for a specific cylindrical shell analyzed and tested by Kriegesmann et al. [11] and Haynie et al. [10]. The shell, which had a probing force imperfection, was loaded axially and subject to fully clamped ends and prescribed end shortening with overall rotation of the ends suppressed. This example will serve to introduce some of the details of the buckling behavior which will be examined in this paper and at the same time it will serve as the reference case for examining other boundary conditions. The shell of Haynie et al. [10], which was analyzed, manufactured, and tested by the authors, has radius $R = 0.2286\,\text{m}$ $(9\,\text{in})$, thickness $t = 1.016$ mm $(0.04\,\text{in})$, $R/t = 225$ and length $L = 0.7874\,\text{m}$ $(31$ in). The shell was modeled as being elastic with Young's modulus $E = 73.08\,\text{GPa}$ $(10.6 \times 10^6\text{psi})$ and Poisson's ratio $\nu = 0.3$. The manufactured test shell had a double joint of width $5.08\,\text{mm}$ $(0.2$ in) at the seam with two strips the thickness of the shell, one bonded on the inside and the other on the outside. This joint is included in our computational model as it was in the models of Refs. [10] and [11]. Otherwise, the geometry of the shell is taken to be that of a perfect cylinder. The boundary conditions for the reference case will be referred to here as case A, and as already noted, these assume each end of the shell is "welded" to a rigid end-plate which forces both the displacements and rotation of the shell to follow the rigid plate along the weld-line. The lower end plate is fixed and the upper end plate is subject to prescribed axial displacement toward lower plate with no overall rotation for case A.

The axial compressive force that develops as the end shortening increases is denoted by F and the lateral probing force imperfection, P, acts in the radial direction pointing inward, as seen in Fig. 1(*a*). In the simulations, the probing force is applied at the midpoint of the shell directly opposite to the joint. In carrying out the simulations, the probing force is first applied reaching the value P and then is not changed as the shell is loaded axially. Simulations for various levels of P are carried out, as will be described. Earlier probing force calculations [11] have shown that the loads for local and global buckling are fairly insensitive to the location of the probe force as long as it is not near the ends or near the joint, and thus the present work will only consider a probe located at the midpoint opposite to the joint.

Our simulations were carried out using Abaqus Standard [20] and quasi-static analysis. The modeling technique followed the one presented in Ref. [10]. The mesh for the models was created by user-written codes and using S4R elements with an element size of $7.112\,\text{mm}$ $(0.28$ in), about $0.5\sqrt{Rt}$, in both axial and circumferential directions. The double joint is included in the model with the elements in that area having a thickness three times the

thickness of the rest of the cylinder. The boundary conditions at the end of the cylinder were applied using the same procedure as in Ref. [10] with rigid links, which connect the central node to the nodes at the end of the cylinder. Geometrically, nonlinear static analysis with automatic stabilization was used, as in Ref. [10], selecting the "specify damping factor option" and a value of 0.0002 for the factor. The adaptive stabilization technique with maximum ratio of stabilization to strain energy was not used. Selected simulations repeated over a range of damping factors (2×10^{-4}, 2×10^{-5}, 2×10^{-6}, 2×10^{-7}, and 2×10^{-8}) revealed essentially no dependence on the damping factor of the results for the local and global buckling loads reported below. For one case reported later, Riks' arc length algorithm was used to compare the results from the automatic stabilization technique to the full equilibrium solution and this comparison also verified the validity of the local and global buckling loads obtained using the quasi-static automatic stabilization technique. For the cases with the probing forces imperfection, each analysis consists of two steps. The first step increases the lateral probing load to the prescribed value with no axial load applied. The second step applies the end shortening (or the axial load) with the probe force held constant.

The relation between the probing force and the inward radial deflection at the probe when the end shortening is zero is plotted in dimensionless form in Fig. 1(*b*) for the shell defined above for case A. The bending stiffness of the shell is $D = Et^3/[12(1-\nu^2)]$. The specific probing force values used in Ref. [10] in performing their buckling calculations are indicated on the curve. To demonstrate concurrence in the two sets of computations, our calculations use the same values plus many additional values. The main features of the simulations are presented in Figs. 2 and 3. To recap, these simulations are performed assuming clamped end conditions with prescribed end-shortening Δ and overall rotation of the ends suppressed. The classical buckling load and associated end shortening for the perfect shell (with $P = 0$) are

$$F_C = \frac{2\pi Et^2}{\sqrt{3(1-\nu^2)}} \quad \text{and} \quad \Delta_C = \frac{tL}{\sqrt{3(1-\nu^2)}R} \tag{2}$$

For the reference shell, these give $F_C = 286.9 \times 10^3$N $(64.49 \times 10^3$ lbs) and $\Delta_C = 2.12$ mm $(0.0834$ in). The end conditions together with the joint modeled in the present simulations produce some differences for the buckling values of the perfect shell from these classical formulas. However, to avoid any ambiguities, the normalizations F/F_C and Δ/Δ_C make use of Eq. (2) for the values F_C and Δ_C in all the figures to follow. Both P and $\delta = w_0$, the associated normal deflection at the probe due to P prior to application of axial loading, will be used as measures of the amplitude of the probing force imperfection.

As noted in the Introduction, four sets of boundary conditions will be considered in this paper. In all four cases both ends of the shell are welded to a rigid end-plate. The lower end-plate is held fixed in all cases. The four conditions on the upper end plate are as follows with the reference case being case A. To our knowledge, all the recent published studies on probing force imperfections have employed case A, which can be regarded as the stiffest of the four. In fact, the papers cited in the Introduction aimed at developing a new approach to knockdown factors for cylindrical shells have all adopted case A. While case A is certainly an important set of end conditions, there are important applications where the overall end rotation is not constrained. In fact, each of the four conditions below can be encountered in applications. Case A is the stiffest loading condition of the four while case D is the most compliant.

$$\left.\begin{array}{ll} \text{Case A:} & \text{prescribed } \Delta \text{ with no overall end rotation} \\ \text{Case B:} & \text{prescribed } \Delta \text{ with no constraint on overall upper end rotation} \\ \text{Case C:} & \text{prescribed } F \text{ with no overall end rotation} \\ \text{Case D:} & \text{prescribed } F \text{ with no constraint on overall upper end rotation} \end{array}\right\} \tag{3}$$

The results of simulations for the reference shell subject to case A conditions are displayed in Figs. 2 and 3. As previously noted, first the probing force P is applied resulting in the normal probe displacement δ. Then, with P unchanged, the end shortening is increased producing changes in axial load F. Our numerical simulations are in excellent agreement with those of Haynie et al. [10], which have been included in Fig. 2. Figure 3, which also closely reproduces a similar plot in Ref. [10], presents details of the load versus end-shortening behavior and the associated development of the probe-induced dimple buckle as a function of end shortening for selected amplitudes of the probing force imperfection. The results for the reference case in Figs. 2 and 3 provide the basis for discussing the behavior associated with probing force imperfections that has emerged in the earlier publications (e.g., see Refs. [5–7], [10], and [11]).

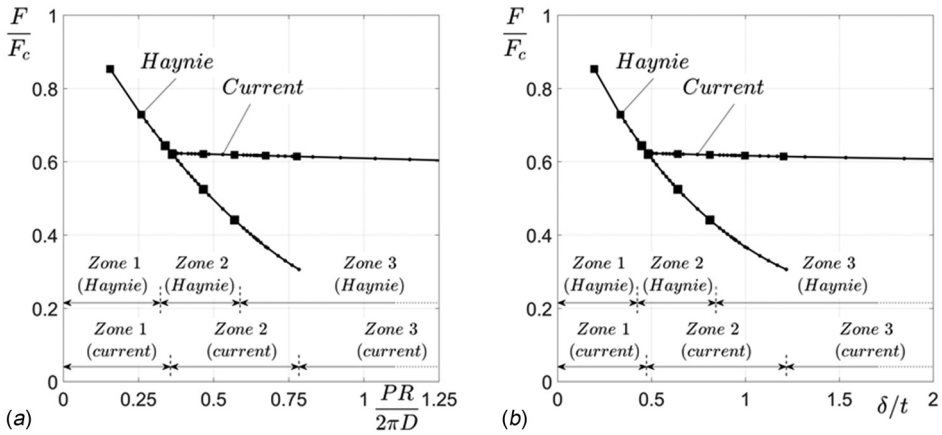

Fig. 2 Local and global buckling loads as a function of the amplitude of the probing force imperfection for the reference shell subject to loading case A. The lower branch of the curves is the local buckling load and the upper branch is the global buckling load. The plots include the results of Haynie et al. [10]. (*a*) The results as F/F_C versus $PR/2\pi D$. (*b*) The same results as F/F_C versus δ/t. The local and global buckling behaviors defining the three zones are discussed in the text.

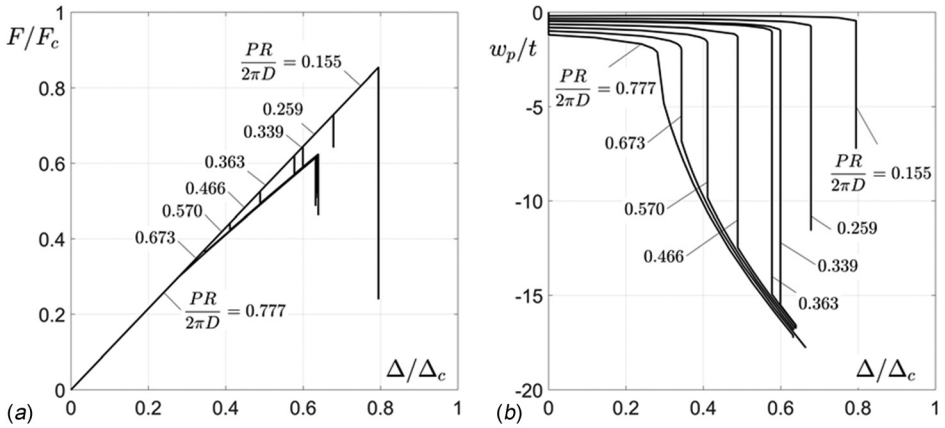

Fig. 3 Further details of the behavior of the reference shell subject to case A conditions. Representative curves of axial load versus end shortening are plotted for several levels of probing force imperfection in (*a*). The associated curves of radial displacement at the probe location versus end shortening are shown in (*b*). The behavior in the three zones is discussed in the text.

For relatively small imperfection amplitudes (e.g., $PR/(2\pi D) < 0.35$ and $\delta/t < 0.5$), in the region denoted as zone 1, the shell buckles globally when the axial load reaches the buckling load plotted in Fig. 1. More precisely, the shell buckles dynamically starting locally in the vicinity of the probe and then spreads around the shell circumference leading to global buckling—in effect, local and global buckling occur simultaneous. Global buckling is accompanied by a large drop in load carrying capacity, as seen in Fig. 3(*a*). The important point is that global buckling in zone 1 is not preceded by *stable* local buckling. For somewhat larger imperfection amplitudes in Fig. 2, in the region denoted by zone 2, as the end shortening is increased, the first buckling event is local buckling: the shell snaps dynamically to form a stable local dimple with a relatively small drop in axial force, c.f., Fig. 3. Then, with further increases in end shortening, the axial load increases to a load above the local buckling load where global buckling occurs accompanied by a large load drop. The overall axial stiffness of the shell in the range between the local and global buckling events is only slightly reduced from the prebuckling stiffness. Zone 3 characterizes behavior for the larger probing force imperfections. The only difference from the behavior in zone 3 from that in zone 2 is that there is no dynamic local buckling event. As seen in Fig. 3(*b*), the dimple at the probe grows monotonically with no dynamic snapping in zone 3 but is otherwise similar in its development to that in zone 2. Moreover, the transition between the global buckling loads in the two zones is smooth. In our view, the important distinction is between zone 1 and the other two zones; practically speaking, zones 2 and 3 can be merged. The ambiguity in the precise boundary between zones 2 and 3 in Fig. 2 is reflected by the fact that the present calculations predict that zone 2 is more extensive than that identified in Ref. [10] due to the larger number of imperfection values evaluated in the present study.

Local buckling in zones 2 and 3 involves significant buckling deflections—5 to 20 times the shell thickness as seen in Fig. 3(*b*)—and the accompanying stresses and strains associated with the local mode must be taken into account if the shell is expected to carry loads above the local buckling load. As has been noted in a number of the earlier studies cited in the Introduction, the global buckling load in zones 2 and 3 is nearly independent of the probing force imperfection amplitude. There have been suggestions that the minimum global buckling load may be the natural choice on which to base the knockdown factor, assuming local buckling can be tolerated. Further insights will emerge when results for the geometric dimple imperfection are presented.

The influence of the end conditions is seen in Fig. 4 where results for the reference shell for each of the four cases in Eq. (3) are plotted against the imperfection amplitude, $PR/2\pi D$, in Fig. 4(*a*) and against the associated amplitude measure, δ/t, in Fig. 4(*b*). There is essentially no difference between case A and case C. In other words, when the overall end rotation is suppressed the loads corresponding to local and global buckling are essentially the same for these two cases. This conclusion is not unexpected because the shell can still support increasing axial load above the local buckling load as the end shortening is increased and thus, prior to global buckling, prescribed axial force and prescribed end-shortening coincide. Figure 4 shows that cases B and D, with no constraint on overall upper end rotation, also have essentially identical local and global buckling loads (for similar reasons). However, while the local buckling load is only slightly reduced from that of cases A and C in zones 2 and 3, the global buckling load is significantly lower (by more than 20%) than the corresponding load for cases A and C. Insight into the reason for the differing effect of end rotation on local and global buckling is provided by Fig. 3(*b*). In zone 1, when local and global buckling are simultaneous, the normal deflection is only on the order of one shell thickness at buckling. This is also true for the onset of local buckling in zones 2 and 3. By contrast, in zones 2 and 3, the dimple deflection can be as much as 20 times the shell thickness when global buckling occurs. End rotation, if allowed, is much more likely to influence behavior at the larger shell deflections than at the smaller ones.

What is not evident in Fig. 4 is that in cases A and B (prescribed end shortening), the shell snaps into a stable buckling pattern encompassing the entire circumference at the global buckling load, while in cases C and D (prescribed axial load), the shell undergoes complete collapse at the global buckling load. In summary, the conclusion to be drawn from the four cases for the reference shell in Fig. 4 is that the effect of overall end rotation on buckling behavior in zone 1 is relatively small (less than 10%) and, similarly, it has a relatively small effect on local buckling behavior in zones 2 and 3. However, allowing overall end rotation significantly reduces the global buckling load in zones 2 and 3 (20% or more).

The effect of the shell length is illustrated in Fig. 5 where results for the stiffest end conditions (case A) are presented in Fig. 5(*a*) and for the most compliant conditions (case D) in Fig. 5(*b*). Other than the end conditions, the only difference among the shells is L where the reference shell analyzed above has $L/R = 3.44$, the shortest shell has $L/R = 1.5$ and the longest shell has $L/R = 5$. The shortest shell has the highest buckling loads, but these results suggest that for shells with the length of the reference shell or somewhat longer, there is relatively little dependence on length. A more extensive study of the effect of L/R for case A

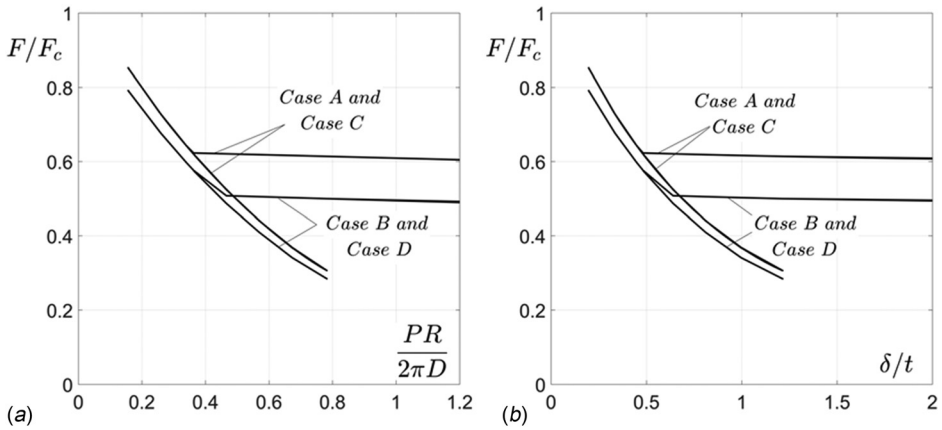

Fig. 4 The roles of the four sets of boundary conditions on local (lower curves) and global (upper curves) buckling of the reference shell. (*a*) Local and global buckling loads as a function of the probing force imperfection amplitude $PR/2\pi D$. (*b*) Local and global buckling loads as a function of the probing force imperfection amplitude δ/t. Cases A and C for which overall upper end rotation is suppressed are essentially identical. Cases B and D for which overall upper end rotation is unconstrained are also essentially identical. Overall end-rotation constraint has relatively little effect on local buckling but significantly effects global buckling in zones 2 and 3.

has been given in Ref. [6] suggesting for even longer shells there may be larger buckling load reductions.

2.1 The Quasi-Static Equilibrium Trajectory, Including the Unstable Portions, and an Inconclusive Analysis of Dynamic Snapping. The numerical method employed to obtain the results described above used a form of artificial damping (called automatic stabilization in ABAQUS) to pass through regions of instability in which the shell undergoes dynamic snapping from one stable equilibrium state to another. Alternatively, in a region of instability, one can make use of the numerical method of Riks [21] in ABAQUS, which identifies a variable that increases monotonically and interchanges its role with the actual load parameter to generate the entire quasi-static equilibrium solution. An illustration of this alternative calculation is presented in Fig. 6 where it is compared to the results obtained using automatic stabilization. The entire equilibrium trajectory generated using the Riks method is more complicated involving excursions with end-shortening reversals, but the important point for present purposes seen in Fig. 6 is that the automatic stabilization procedure correctly captures the drop in load from one state to another associated with the unstable buckling event under prescribed end shortening.

Another question that should be asked is whether the snapping event that occurs at a point of instability might lead to dynamic "overshoot" such that the local buckling event departs significantly from the equilibrium curve obtained by the quasi-static method and even triggers global buckling. If this were to occur, it would seem most likely to take place under a prescribed axial load. An investigation of this question requires a dynamic simulation accounting for shell inertia. We have used ABAQUS Explicit to preform selected calculations for end conditions case A and case D assuming the shell material has the density of aluminum. The rigid end-plates were considered to be massless and the prescribed end shortening, or prescribed axial force, were increased linearly at a slow rate such that prebuckling dynamic effects are very small. The results of our simulations for the global buckling loads for the reference shell were inconclusive and we recommend that further dynamic simulations be carried out. Specifically, our dynamic simulations have been unable to validate with any confidence the quasi-static prediction of a regime where local snap buckling leads to a stable dimple buckle followed by global buckling at a higher axial load. The possibility that the dynamic local buckling event triggers global buckling without an additional increase of axial load has not yet been ruled out. It should be noted however that the shells fabricated and tested by Haynie

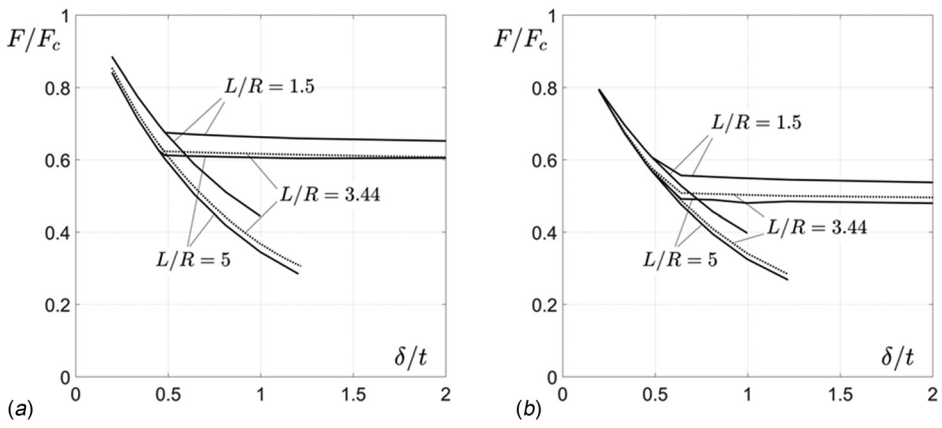

Fig. 5 The influence of the shell length for the case of probing force imperfections for case A in (*a*) and case D in (*b*). The parameters characterizing the three shells are the same as for the reference shell except for their length *L*. The reference shell has $L/R = 3.44$.

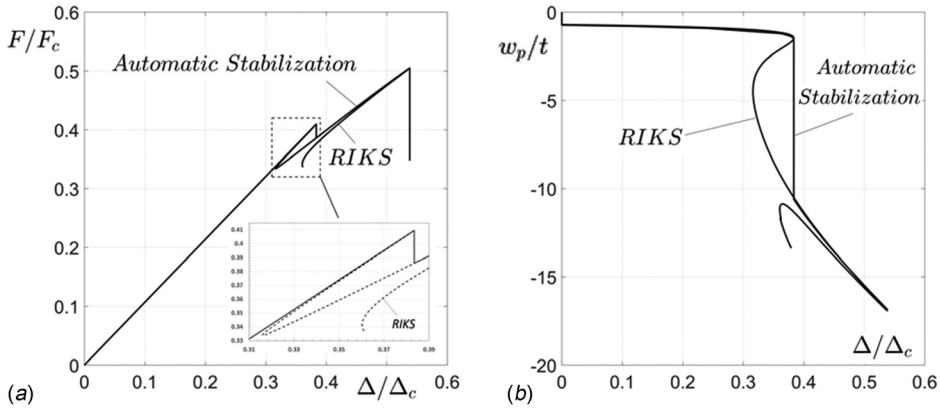

Fig. 6 Full equilibrium solution generated using the Riks method compared to the results using automatic stabilization. (*a*) Load versus end shortening and (*b*) normalized inward displacement to the shell, w_P/t, at the probe force location versus end shortening. Reference shell with case A boundary conditions and $PR/2\pi D = 0.570$.

et al. [10] behaved in accord with their finite element analyses especially when a small amount of overall end rotation was taken into account.

3 Experimental Study Probing an Axially Compressed Cylinder With or Without End-Rotation Constraint

Here, we study experimentally the probing response of a clamped shell tested under prescribed end shortening with no end rotation (case A), and the same shell tested with end rotation allowed (case B). The lateral probe employed in these experiments is a nondestructive experimental device used to reveal the landscape relevant to buckling [22]. The three shells tested in the experimental programs had moderately large geometric imperfections acquired in the manufacturing process such that each buckled at loads around 30% of the classical buckling load.

3.1 Experimental Setup. The experiments were conducted with commercial aluminum cylindrical shells (empty coke cans) of radius $R = 28.6$ mm, thickness $t = 0.104$ mm (radius-to-thickness ratio $R/t = 274$) and a total height $L = 107$ mm. We use a custom-made biaxial machine (ADMET Inc., Norwood, MA) to accurately compress each shell and simultaneously probe them in the midplane, as shown in Fig. 7(*a*). The vertical axis has a resolution of 20 μm in displacement and 0.1 N force with a maximum force of 2200 N. A blunt probe is installed in the horizontal axis, which also has a 20 μm displacement resolution. The probe tip is a steel marble of diameter 4.7 mm. The probe force is measured by an S-beam load cell with 5 mN resolution and a maximal load of 100 N. The axes of the machine are analog-controlled with an acquisition card NI DAQ USB-6001.

Two sets of boundary conditions in the experiments closely approximate two of those considered in Sec. 2: case A, prescribed end shortening with no overall end rotation; and case B, the same shell tested with overall end rotation allowed. The difference between case B and case A is the addition of a pair of 2 mm thick steel plates at the top end of the shell, with a steel marble of diameter 4.8 mm between the plates, as shown in Fig. 7(*c*). Small, shallow excavations at the center of each of the plates keep the marble centered and allow the top end of the can to undergo overall rotation. Three cans were tested with similar results to those described below for one of the cans.

3.2 Probing of the Landscape of Stability of the Shell With or Without End-Rotation Constraint. The shell is incrementally compressed by steps of 10–20 μm in the axial direction. At each step, the end shortening is held fixed and the horizontal probe is advanced toward the shell at a constant speed 6 mm/min, as in Fig. 7(*a*). The probing displacement d ranges from 0 to 1.5 mm. For axial loads larger than 600 N, the probing is interrupted once a maximum of the probing force–displacement curve is detected. This prevents buckling events or plasticity triggered by the probing and thereby permits repeated probing of the shell [22]. For similar reasons, axial loads larger than 1000 N were not imposed.

The range of axial load F covered by the procedure is approximately 400–1000 N, while the range of the measured probing force P is almost three orders of magnitude smaller. The probing technique reveals a landscape of stability, as shown in Fig. 8. Following [22], we call "ridge" and "valley" the trajectory of the maxima and minima of probing force, respectively. The ridge and the valley are, respectively, denoted by squares and circles in Fig. 8. We also indicate the trajectory of the projection of the

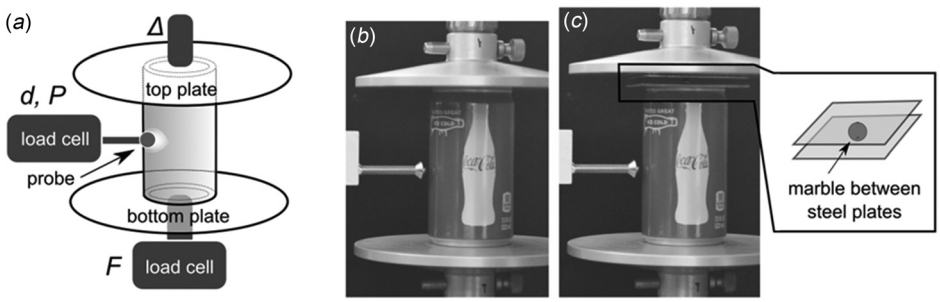

Fig. 7 (*a*) Schematics of the experimental setup. (*b*) Prescribed end shortening with no end rotation (case A). (*c*) Prescribed end shortening with end rotation allowed (case B). The rotation is enabled by two steel plates with a steel marble located at the center of the top end of the shell, as shown in the schematic on the right.

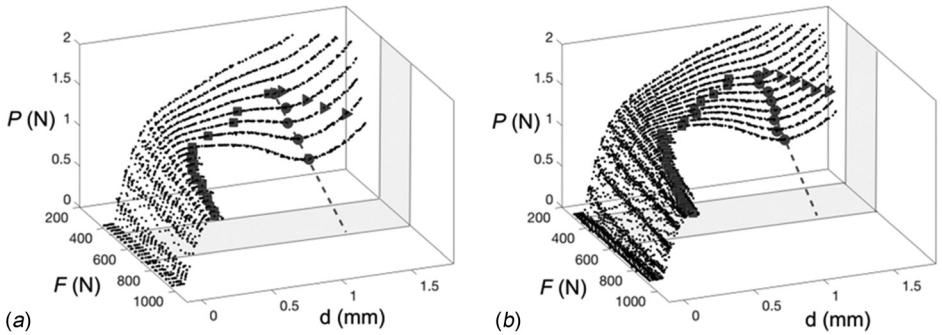

Fig. 8 (*a*) Landscape of stability of the shell without end rotation (case A). (*b*) Landscape of the same shell with overall end rotation allowed (case B). The squares, circles and triangles are, respectively, the ridge, valley, and projection of the ridge on the opposite face of the valley. The gray area indicates the range of axial loads where a valley is found in the landscape (values estimated by linear extrapolation).

ridge on the other face of the valley: in a load-controlled probing experiment, the probe would jump suddenly from the ridge (squares) to the projection of the ridge (triangles). This is of fundamental importance to understand the difference between local and global buckling. As noted above, probing beyond the ridge for axial loads of above about 600 N in Fig. 8 was not conducted for fear of triggering buckling deflections so large that the shells would be irreversible damaged.

In order to facilitate the interpretation of the probing data, the two landscapes of Fig. 8 are projected onto the plane $(d/t, F)$ in Figs. 9(*a*) and 9(*b*) and onto the plane (F, P) in Figs. 9(*c*) and 9(*d*). As the probe displacement is changed from $d/t = 0$ to $d/t = -20$ in Fig. 9(*a*), the probe either crosses the valley of the landscape ($456\,\text{N} < F < 693\,\text{N}$: values are estimated by linear extrapolation), or do not reach any valley ($F < 456\,\text{N}$ or $F > 693\,\text{N}$). The three ranges (prevalley, valley, and postvalley) are marked in Figs. 9(*a*) and 9(*b*) by vertical straight lines. A load-controlled probe crossing the valley would jump from buckling deflections in the range $d/t = 2 - 10$ to a value in the range $d/t = 10 - 16$, depending on the precise value of F, consistent with the magnitude of the buckling jumps predicted in Fig. 3(*b*).

By comparing Figs. 9(*a*) and 9(*b*), one sees that the valley for the shell with no constraint on upper end rotation is shifted to lower values of axial loads by about 15%, from (456–693 N) to (351–596 N). A similar drop in the axial loads associated with the landscape ridge occurs. When the axial force (now on the vertical axis) is plotted as a function of probing force in Figs. 9(*c*) and 9(*d*), the three regimes of the axial loads in the landscape (prevalley, valley, postvalley) dictate the types of buckling that can occur analogous to those discussed in Fig. 4. The valley regime gives rise to "local buckling" mapped in Figs. 9(*c*) and 9(*d*), with a dimple buckle developing beyond the ridge as the shell is probed. At axial loads below the valley regime, buckling due to probing does not occur. At axial loads above the valley regime, global buckling

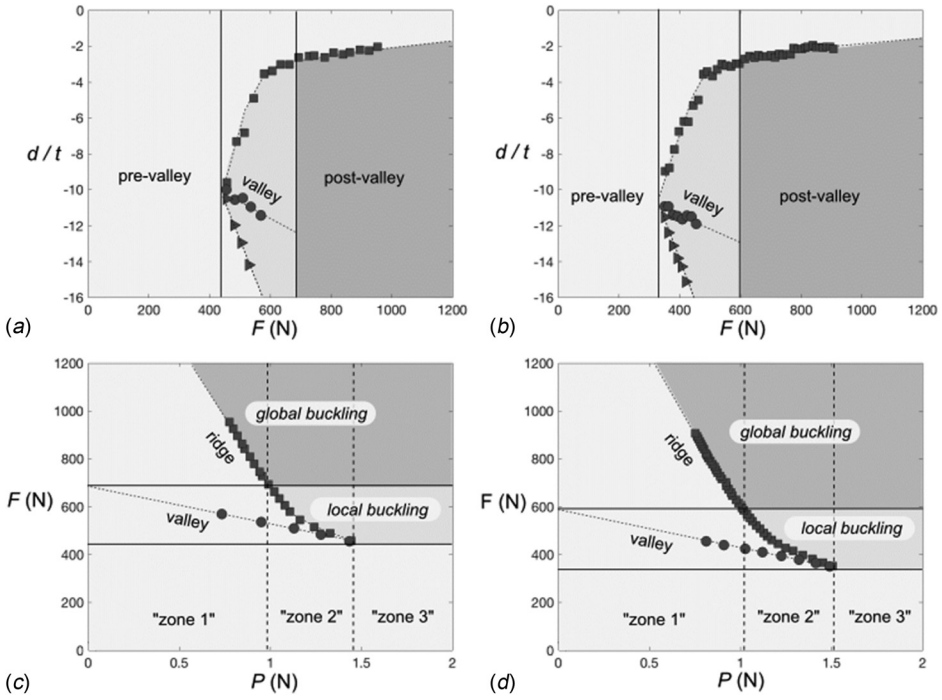

Fig. 9 (*a*) Projection of the landscape of stability in the plane containing the probing displacement with the axial force as the horizontal axis, case A. (*b*) The same for case B. (*c*) Projection in the plane containing the probing force with the axial force as the vertical axis, case A. (*d*) The same for case B.

will occur at some probe displacement beyond the ridge. The lines demarking the three regimes and three zones in Fig. 9 are not necessarily straight lines as has been sketched in the figure.

In summary, the experiments on this shell, which are representative of those of the other two shells tested, reveal that relaxing the constraint on overall end rotation reduces the axial loads associated with the ridge and valley of the buckling landscape by roughly 15%, roughly consistent with what one would expect from the results in Sec. 2. While it has not yet been possible to measure the global axial buckling loads for the two cases by probing, we expect these reductions in axial load will be representative of the buckling load reductions.

4 Elastic Buckling Behavior of Cylindrical Shells Under Axial Compression in the Presence of Local Geometric Dimple Imperfections

Given the apparent widespread agreement in the buckling community that highly correlated imperfection patterns covering the entire shell are not realistic for cylindrical shells under axial compression, there has been surprisingly little published work on more realistic localized geometric dimple imperfections. An important exception is the contribution of Wullschleger [19] in Chap. 6 of his Ph.D. thesis, which is not otherwise published. Wullschleger primarily considered the stiffest set of boundary conditions, case A, but he also considered an alternative set of conditions which will be mentioned later. The form of the geometric, stress-free dimple imperfection assumed in Ref. [19] has for the initial normal inward deflection (in our notation)

$$w_I(x,y) = \frac{\delta}{4}\left\{1+\cos\left[\frac{\pi(x-x_0)}{\ell_x}\right]\right\}\left\{1+\cos\left[\frac{\pi(y-y_0)}{\ell_y}\right]\right\} \tag{4}$$

for $|x-x_0| \le \ell_x$ and $|y-y_0| \le \ell_y$ with $w_I = 0$ otherwise. The coordinates (x,y) run in the circumferential and axial directions, respectively, with the imperfection centered at (x_0, y_0). The amplitude of the dimple imperfection is δ.

We begin by discussing results for the limit of an *axisymmetric dimple* given by Eq. (4) with $\ell_x \to \infty$, i.e.,

$$w_I(x,y) = \frac{\delta}{2}\left\{1+\cos\left[\frac{\pi(y-y_0)}{\ell_y}\right]\right\} \text{ for } |y-y_0| \le \ell_y \tag{5}$$

and $w_I = 0$ otherwise. Results for the axial buckling load for the *axisymmetric geometric dimple imperfection* (5) have been presented in Ref. [19] and in 1971 by Hutchinson et al. [23] for boundary conditions corresponding to case A with the imperfection located at the center of the shell. The two sets of predictions are in close agreement. The 1971 paper compares the numerical predictions with experiments on photoelastic epoxy spun-cast cylindrical shells containing precisely machined dimple imperfections of the form (5). Two figures from the earlier paper are presented here in Fig. 10.

In Fig. 10(*a*), the axial half-wavelength of the machined dimples and those in the simulations was taken to be $\ell_y = 1.05\ell_C$ where

$$\ell_C = \pi\sqrt{\frac{Rt}{\sqrt{12(1-\nu^2)}}} \tag{6}$$

is the half-wavelength of the classical axisymmetric buckling mode of the cylindrical shell under axial compression. For an imperfection amplitude fixed at $\delta/t = 0.363$, Fig. 10(*b*) shows the influence on the buckling load of the dimple half-wavelength, ℓ_y. A dimple with $\ell_y \cong \ell_C$ produces the near-minimum buckling load. These figures include the prediction from an asymptotic formula for this imperfection obtained by Amazigo and Budiansky [24]. Details of the calculations and the experiments are provided in Ref. [23]. At the loads recorded in Fig. 10, the test shells buckled globally with a significant drop in load carrying capacity, as would be expected because the axisymmetric dimple triggers buckles encircling the entire shell. For this imperfection, there is no separation between global and local buckling.

The reader is referred to the thesis of Wullschleger [19] for his thorough study of the buckling of cylindrical shells with the localized dimple imperfection (4). That study examines the roles of the two dimple wavelength parameters, ℓ_y and ℓ_x, and reveals the existence of local buckling followed by global buckling at a higher load similar to that which occurs for the probing force imperfections. In what follows, we present the results of our own study, which allows a direct comparison with results for the probing force imperfection in Sec. 2 and which emphasizes the role of the four sets of boundary conditions (3). In the present work, a slightly different dimple imperfection shape from that in Eq. (4) is assumed

$$w_I(x,y) = \delta\, e^{-[(x-x_0)/\hat{\ell}_x]^2 - [(y-y_0)/\hat{\ell}_y]^2} \tag{7}$$

which is exponentially small well away from the imperfection center at (x_0, y_0). For the axisymmetric imperfection ($\hat{\ell}_x \to \infty$), this shape is approximately equivalent to that in Eq. (5) if $\hat{\ell}_y = 0.55\ell_y$. In the simulations presented below, the same reference shell used for the probing force imperfection study will be invoked, and the dimple imperfection center has been located at the midpoint of the shell directly opposite the joint. Figure 11 provides a comparison of shapes of the dimple imperfection with that of the probing force imperfection at the same value of imperfection amplitude δ. Recall that for the probing force imperfection, δ is defined as the deflection due to the probe force prior to application of the axial load.

Figure 12 presents a comparison of the buckling behavior of the reference shell with the geometric dimple imperfection (4.4) (with $\hat{\ell}_y = 0.55\ell_C$ and $\hat{\ell}_x/\hat{\ell}_y = 2$) with the buckling behavior of the same shell with the probing force imperfection. Comparisons for each of the four end conditions have been determined, and a plot using the normalized imperfection amplitude measure δ/t is presented for both types of imperfections. There is a close parallel in the behaviors for the two types of imperfections. Zone 1 exists for both types in the regime of smaller imperfection amplitudes in which local and global buckling occur simultaneously. Zone 2 exists in which local buckling precedes global buckling with an appreciable gap in axial load between the two for cases A and C end conditions. When overall end-rotation constraint is absent in cases B and D, the axial load gap between local and global buckling is smaller. A similar reduction in the spread between local and global buckling was observed in Ref. [19] for boundary conditions, referred to as CC3, which assumed a uniform axial resultant stress at the upper end of the shell, which also offers no constraint on overall end rotation. Both imperfection types also exhibit zone 3 behavior in which local snap buckling is replaced by a more gradual growth of the nascent dimple buckle. An important feature brought out by these comparisons is the near-coincidence of the plateau load at which global buckling occurs for the two types of imperfection—this near-coincidence holds for each of the four end conditions. A geometric dimple imperfection gives rise to the same drop in global buckling load due to the relaxation in overall end-rotation constraint that occurs for the probing force imperfection. Equally important is the fact that the significant drop in global buckling load in zones 2 and 3 when there is no constraint on overall end rotation occurs for both types of imperfection. One also notes that local buckling is much less affected by end-rotation constraint for both types of imperfections, including in zone 1 where the local and global buckling loads are coincident.

There are, however, differences between the buckling predictions for the two types of imperfection. The boundaries between

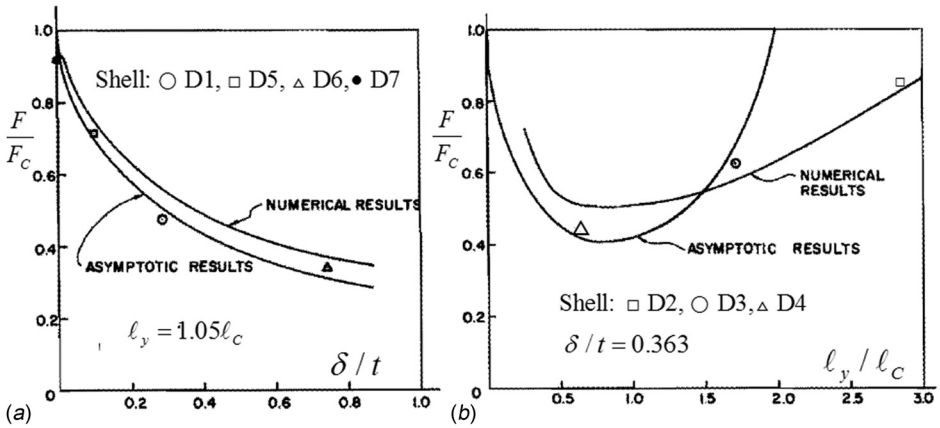

Fig. 10 Comparison between buckling theory and experiments for cylindrical shells under axial compression with an axisymmetric dimple imperfection (5) located at the shell midsection and subject to case A end conditions (adapted from Ref. [23]). (*a*) Global buckling load as dependent on imperfection amplitude for $\ell_y = 1.05\ell_C$. (*b*) Global buckling load as dependent on the dimple wavelength for a fixed imperfection amplitude, $\delta/t = 0.363$. The calculations were performed for a shell with $R/t = 200$, $L/R = 2.8$ and $\nu = 0.4$, values very close to those measured for the test specimens as discussed in the original paper.

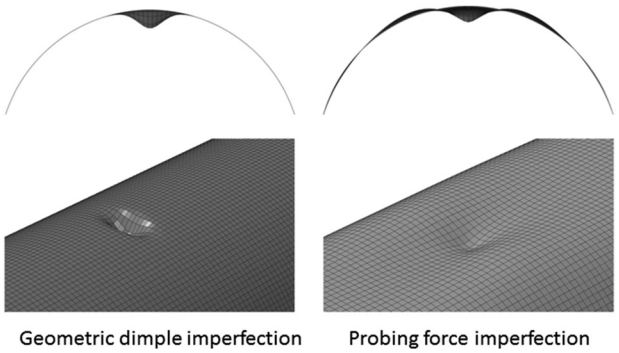

Fig. 11 Shapes of the geometric dimple imperfection ($\hat{\ell}_y = 0.55\ell_C$, $\hat{\ell}_x/\hat{\ell}_y = 2$) and the probing force imperfection at the same imperfection amplitude δ

zone 2 and zone 3 differ, but as discussed earlier, this is not likely to be important. More significant is the fact that lower local buckling loads are predicted for the probing force imperfections in the range of "larger" imperfections with $\delta/t > 0.5$. Whether these lower loads are realistic depends on whether probing force imperfections are representative of actual imperfections. In the range of smaller imperfections, it is possible to define a correspondence between the amplitudes of the two types of imperfections, but not in the range of the larger imperfections. If the actual imperfection is not due to a probing force but if, instead, a geometric dimple imperfection is more realistic, then the prediction based on the probing force imperfection will be significantly overly conservative when $\delta/t > 0.5$.

Figure 13 reveals further details of the correspondence in buckling behavior for the two types of imperfections. This figure that is plotted for case A end conditions can be compared with the earlier plot for probing force imperfections in Fig. 3. The similarity in nonlinear responses is striking, including the fact that for both types of imperfections local buckling will generally involve lateral deflections in the range from about 10–20 times the shell thickness. If local buckling is to be tolerated, designs will necessarily have to consider the stresses and strains associated with the local buckles.

The effect of different axial widths of the dimple imperfection on buckling is qualitatively similar to that seen in Fig. 10(*b*) for the axisymmetric dimple imperfection. For a given ℓ_x the choice

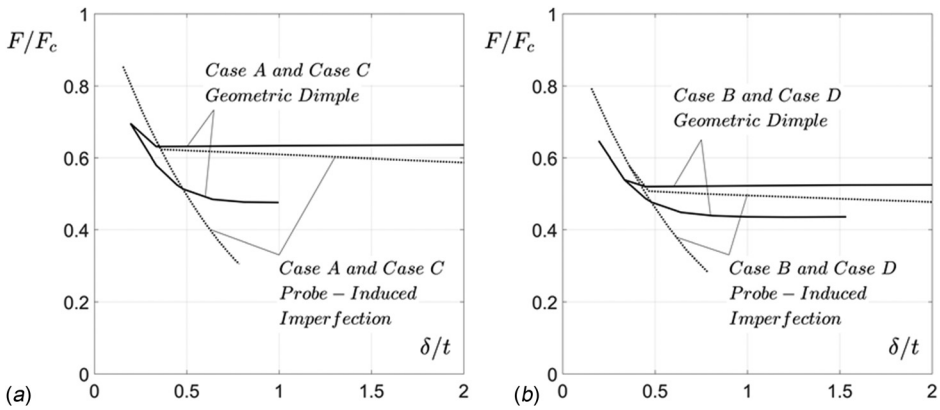

Fig. 12 Local and global buckling for the reference cylindrical shell with the local dimple imperfection (4.4) ($\hat{\ell}_y = 0.55\ell_C$ and $\hat{\ell}_x = 2\hat{\ell}_y$) compared with corresponding results from Sec. 2 for the probing force imperfections. Results for the four sets of end conditions (3) are presented: (*a*) Case A and C, which are nearly identical. (*b*) Case B and D, which are nearly identical.

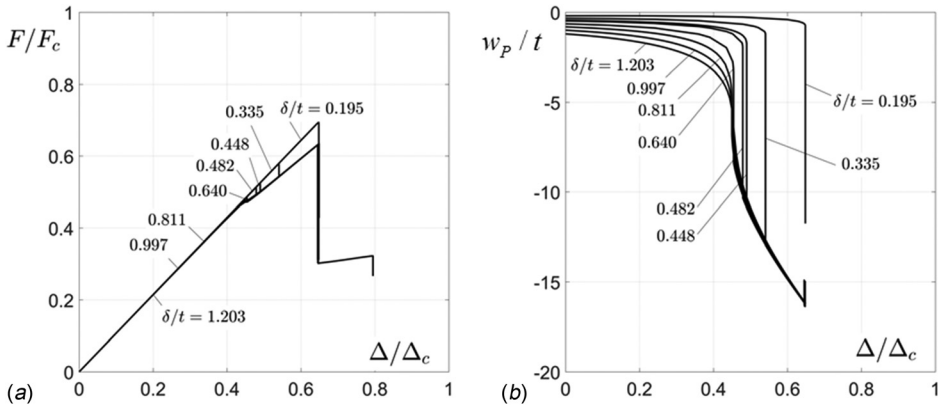

Fig. 13 Nonlinear buckling behavior for the reference cylindrical shell with the local dimple imperfection (7) with $\hat{\ell}_y = 0.55\ell_C$ and $\hat{\ell}_x = 2\hat{\ell}_y$ subject to case A end conditions

$\hat{\ell}_y = 0.55\ell_C$ gives the near-minimum local buckling load, and for modest changes away from $\hat{\ell}_y = 0.55\ell_C$ there is very little change in this buckling load. The global buckling load was also found to be relatively insensitive to the shape and size for dimples characterized by wavelengths not too different from $(\hat{\ell}_x/\hat{\ell}_y = 2,\ \hat{\ell}_y = 0.55\ell_C)$. Additional studies on the influence of dimple imperfection size and shape based on Eq. (4) are given in Ref. [19].

The transition from the type of behavior seen in Figs. 12 and 13 to dimples whose circumferential length is sufficiently long that the shells buckle at axial loads close to those for the axisymmetric dimple imperfections is seen in Fig. 14. This figure reveals the influence of the dimple imperfection aspect ratio $\hat{\ell}_x/\hat{\ell}_y$ on the imperfection-sensitivity for imperfections with $\hat{\ell}_y = 0.55\ell_C$ for the reference shell with case A end conditions. The curves record the first buckling event as the end shortening is increased from zero. For small imperfection amplitudes, there is very little dependence on the aspect ratio of the dimple and the lowest buckling load is nearly the same as that of the axisymmetric dimple imperfection. However, as noted above, the dimples with the smaller aspect ratio first undergo local buckling and then at a higher load undergo global buckling. At larger imperfection amplitudes, the aspect ratio of the imperfection has more influence with the larger aspect ratios, e.g., $\hat{\ell}_x/\hat{\ell}_y > 4$, giving rise to buckling only slightly above the prediction for the axisymmetric dimple imperfection. For the smaller aspect ratios, e.g., $\hat{\ell}_x/\hat{\ell}_y = 2$ and 3 in Fig. 14, the buckling load plateaus at a value of F/F_C slightly below 1/2 as the imperfections become large.

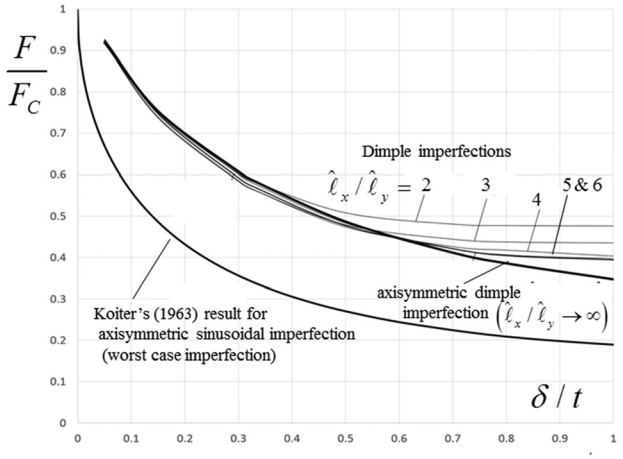

Fig. 14 Buckling imperfection-sensitivity curves for geometric dimple imperfections compared to Koiter's [16] worst case imperfection, the axisymmetric sinusoidal imperfection with $\nu = 0.3$. The lowest buckling loads are plotted for localized dimple imperfections (7) having aspect ratios ranging from $\hat{\ell}_x/\hat{\ell}_y = 2$ to ∞ (the axisymmetric limit). For all the dimple imperfections, $\hat{\ell}_y = 0.55\ell_C$. The curves for the dimple imperfections have been computed for the reference shell but they are essentially independent of R/t. Koiter's curve is independent of R/t.

An early study by Berry and Rotter [18] investigated the transition from a local dimple imperfection to an axisymmetric dimple imperfection for a shell with $R/t = 800$ and found that the buckling load of a shell with a dimple imperfection nearly coincided with the axisymmetric limit when it reached a circumferential extent of about 40 deg. The reference shell in Fig. 14 has $R/t = 225$. We have repeated the dimple imperfections calculations presented in Fig. 14 for two other shell thicknesses keeping the radius unchanged, corresponding to shells with $R/t = 100$ and $R/t = 50$, and scaling the dimple imperfection lengths consistent with the thickness dependence of ℓ_C in Eq. (6). There is too little difference between the dimple imperfection-sensitivity curves for these two other R/t values from those in Fig. 14 to justify presenting them. The results in Fig. 14 are essentially independent of R/t, to a good approximation. It should also be noted that the reference shell on which the dimple results in Fig. 14 are based has the double joint which raises the value of F/F_C buckling load by a few percent because the normalizing factor F_C in Eq. (2) does not account for the joint.

Koiter's [16] imperfection-sensitivity curve for a sinusoidal axisymmetric geometric imperfection covering the entire shell is included in Fig. 14. (This shell has no joint.) The axial variation of the radial displacement of the imperfection is $w_I(y) = \delta\cos(\pi y/\ell_C)$. Based on his general asymptotic theory, Koiter [15] showed that this imperfection is the most degrading. For amplitude δ, the sinusoidal axisymmetric imperfection is generally regarded as the worst case imperfection. Koiter's curve in Fig. 14 is not an asymptotic analysis but instead is based on an accurate solution for finite δ. It is independent of R/t. Moreover, Koiter's load coincides with the onset of dynamic snap buckling for values of F/F_C greater than about 0.2 [25].

The imperfection-sensitivity curves in Fig. 14 appear to span the range of buckling knockdowns envisioned in the current efforts to revise the knockdown factors for unstiffened cylindrical shells under axial compression. The knockdowns depend on the imperfection amplitude, δ, and on whether the imperfection is local or wide-spread and highly correlated. The loads in Fig. 14 denote the first buckling event encountered as the axial load is increased, whether it be local or global buckling. The ratio F/F_C for the first buckling event is essentially independent of R/t and has very little dependence on L/R if the shell's length is significantly greater than the width of its two end boundary layers. As has also been shown here, the first buckling event has a relatively small dependence on which of the four end conditions considered

here apply—never more than about a 10% difference between the stiffest end conditions, case A, and the most compliant, case D. We return to the implications of Fig. 14 in the final discussion in Sec. 6.

5 The Buckling of Spherical Shells Under External Pressure in the Presence of Geometric Dimple Imperfections or Probing Force Imperfections: Comparison With the Behavior of Cylindrical Shells Under Axial Compression

This section draws from recent work [26–28] on the imperfection sensitivity of spherical shells and reports results for the same two types of imperfections considered for the cylindrical shells: geometric dimple imperfections and probing force imperfections. The results are for full spheres with either identical geometric dimple imperfections at the upper and lower poles or with equal and opposite probing forces applied at the poles. The shells are assumed to deform axisymmetrically with symmetry about the equator. Had the shells been taken to be hemispherical with clamped conditions at the equator, essentially identical results to those reported below would have been obtained because the interaction between the buckle at the pole and the equator is extremely weak. It will be seen that the behavior of the spherical shells is quite different from that reported for cylindrical shells under axial compression in several important respects. The differences in the behaviors serve notice that any protocol for establishing knockdown factors will have to depend on the specific shell/loading combination. Furthermore, further evidence will emerge suggesting that a probing force may not be an effective surrogate imperfection.

For the probing force imperfection, equal and opposite normal pole forces, P, are first applied to the shell prior to application of external pressure p. The response with $p = 0$ is presented in Fig. 15. In what follows, we will use $PR/(2\pi D)$ and $\delta/t \equiv w^0_{\text{pole}}/t$, as convenient, for measures of the amplitude of probe force imperfection where w^0_{pole} is the inward deflection at the pole due to P with $p = 0$.

With the probing force P held constant, the external pressure p is increased until the shell buckles. For spherical shells deforming axisymmetrically, overall rotation is not an issue, but the distinction between prescribe volume change or prescribe pressure is important, as will be seen. Prescribed volume change can be achieved in the laboratory by filling the shell with a fluid that is effectively incompressible and then withdrawing the fluid in a controlled manner thereby inducing a net external pressure. Prescribed volume change is also referred to as rigid pressure loading. At the other extreme is the most compliant loading wherein the loading system maintains a prescribed pressure independent of the shell deformation. The two loading conditions are analogous, but not fully comparable, to prescribed end shortening and prescribed axial force for cylindrical shells. The nonlinear buckling behavior of spherical shells for the two limiting cases of prescribed pressure and prescribe volume change will be presented. The numerical method employed for solving the nonlinear axisymmetric shell problem is the same as that used in Refs. [26–28]. For the probing force imperfections, the results have been computed for geometrically perfect spherical shells.

For both prescribed pressure and prescribed volume change, the inward pole deflection increases monotonically as the shell deforms and buckles. The calculations were carried out by prescribing increments of pole deflection and computing the corresponding increments of p or volume change ΔV—effectively a Riks method with pole deflection as the monotonically changing "load parameter." Curves of the pressure as a function of pole deflection are plotted in Fig. 16(*a*) for various levels of probing force imperfection for the case in which the shell volume is unconstrained. The companion curves for the variation of the volume change are plotted in Fig. 16(*b*). In Fig. 16, $\Delta w_{\text{pole}} = w_{\text{pole}} - w^0_{\text{pole}}$ is the additional inward pole deflection associated with application of p. The classical buckling pressure and associated volume change for the full perfect sphere with $P = 0$ are

$$p_C = \frac{2\,(t/R)^2}{\sqrt{3(1-\nu^2)}} \quad \text{and} \quad \Delta V_C = \frac{4\pi(1-\nu)R^2 t}{\sqrt{3(1-\nu^2)}} \tag{8}$$

The behavior as predicted by the curves in Fig. 16 will first be discussed for prescribed pressure and then for prescribed volume change.

For *prescribed pressure,* the loading system applies the pressure in such a way that even if the shell buckles the pressure is maintained constant. The volume of the shell is unconstrained and changes according to Fig. 16(*b*). It is obvious from Fig. 16(*a*) that under prescribed pressure, for any of the curves for the probing force imperfections plotted, the shell undergoes complete collapse when the pressure reaches the maximum pressure $p_{\max}$. The spherical shell collapses until the opposite poles make contact [26]—in other words, when $p_{\max}$ is attained the shell snap buckles and is "smashed." The relation between the maximum pressure and the probing force imperfection amplitude is plotted in Fig. 17(*a*). It is important to the discussion later related to prescribed volume change that it is understood that buckling under prescribed pressure in Fig. 17 is associated with complete collapse of the shell.

Included in Fig. 17(*a*) is the curve for the normalized buckling pressure, $p_{\max}/p_C$, associated with a geometric dimple imperfection at the poles whose initial, stress-free shape is given by the inward radial deflection

$$w_I = \delta e^{-(\beta/\beta_I)^2} \text{ with } \beta_I = B\sqrt{\frac{t/R}{\sqrt{1-\nu^2}}} \tag{9}$$

Here, δ is the amplitude of the geometric dimple imperfection, β is the angle measured from the pole and B is a value on the order of unity for the most deleterious imperfections (see Refs. [26] and [27] for details on the dependence on B and the fact that β_I in Eq. (9) ensures that $p_{\max}/p_C$ is independent of R/t). The trends for the geometric and probe force imperfections are qualitatively similar,

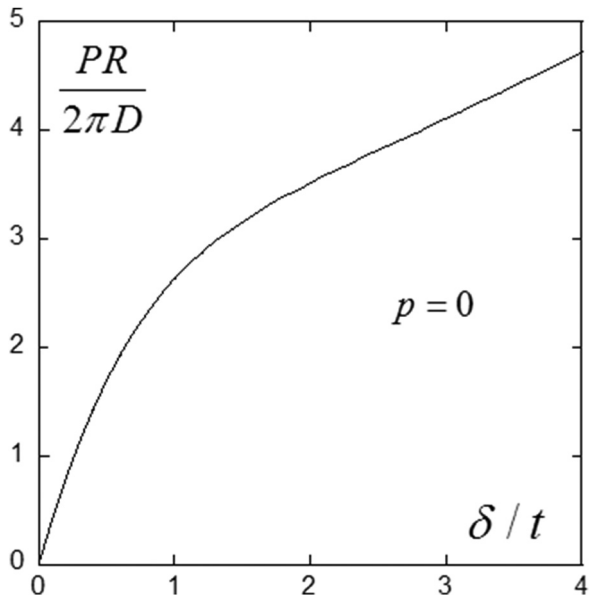

Fig. 15 Dimensionless relation between the pole probing force, *P*, and the inward deflection at the pole, $\delta = w^0_{\text{pole}}$, computed with $p = 0$ for $R/t = 200$ and $\nu = 0.3$. Over the range plotted the curve would be essentially identical had it been computed under a constraint of no volume change. These results are independent of *R/t* but they do depend on ν.

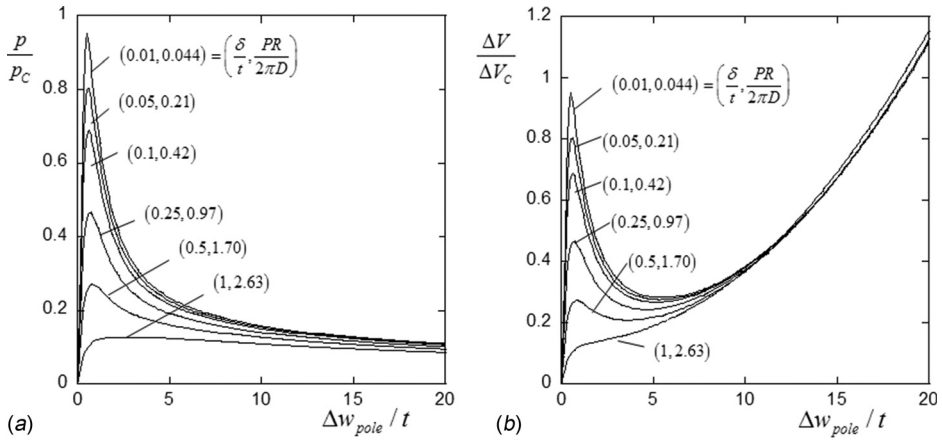

Fig. 16 Nonlinear response of the spherical shell with *P* held fixed with subsequent application of external pressure *p* for six levels of surrogate probing force imperfections characterized by ($\delta/t, PR/2\pi D$). (*a*) p/p_C versus pole deflection $\Delta w^0_{pole}/t$. (*b*) normalized volume change $\Delta V/\Delta V_C$ versus $\Delta w^0_{pole}/t$. The results can be used to generate behavior for both prescribed pressure and prescribed volume change, as will be discussed in the text. These have been computed with $R/t = 200$ and $\nu = 0.3$, but the results in (*a*) are independent of R/t. The results in (*b*) have some dependence on R/t.

although differences are evident in the range of larger imperfections. As for the probing force imperfection, under prescribed pressure the shell with the geometric dimple imperfection undergoes snap buckling and complete collapse when p_{max} is attained. A comparison of the theoretical imperfection-sensitivity prediction for the dimple imperfection minimized over B with experiments on elastomeric hemi-spherical shells clamped at the equator is presented in Fig. 17(*b*) taken from Ref. [27]. The shells in the experiments had precisely manufactured dimple imperfections represented by Eq. (9) with amplitude δ. Further details of the experimental and theoretical imperfection-sensitivity studies are presented by Lee et al. [27].

Now, consider external pressure applied by *prescribing the reduction in volume* of the spherical shell following the imposition of the probing force imperfection P. In this case, ΔV in Fig. 16(*b*) is increased until the first local peak, ΔV_{max}, is attained, assuming a local peak exists. At this point the shell becomes unstable and undergoes snap buckling, maintaining constant ΔV, to the stable buckled state on the right hand side of the curve at $\Delta V = \Delta V_{max}$ in Fig. 16(*b*). To an excellent approximation, the maximum pressure and volume change for a given level of imperfection satisfy $\Delta V_{max}/\Delta V_C \cong p_{max}/p_C$, whether the loading is prescribed pressure or prescribed volume change, simply because these peak values are attained at very small deflections, i.e., $\Delta w_{pole}/t \approx 1$ in Fig. 16. Thus, with one caveat mentioned shortly, there is very little difference between the two limiting loading conditions, prescribed pressure and prescribed volume change, on the maximum pressure the shell can support prior to buckling. The results for the buckling pressure for both geometric and probing force imperfections in Fig. 17 apply equally well to the two limiting loading conditions except for larger imperfections, as will be discussed. The near-simultaneity of the peak buckling pressure under the most rigid and most compliant loading conditions has been known for many decades.

There is, however, a dramatic difference in the post-buckling behavior for the two loading cases [28]. As emphasized earlier, under prescribed pressure, the shell collapses completely when p_{max} is attained. By contrast, under prescribe volume change, the shell snaps to a state with a stable dimple buckle. The pole deflection of the buckle lies in the range $10 < \Delta w_{pole}/t < 20$, depending

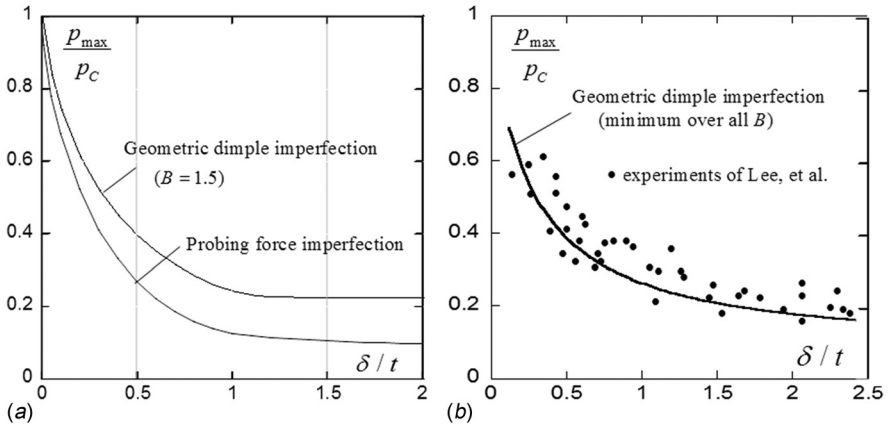

Fig. 17 (*a*) Buckling imperfection-sensitivity for special shells under prescribed external pressure for both probing force imperfections and geometric dimple imperfections with $B = 1.5$. These theoretical curves have been computed with $R/t = 200$ and $\nu = 0.3$ but they are essentially independent of R/t. (*b*) Imperfection-sensitivity prediction for geometric dimple imperfections minimized over B and comparison with the experiments on clamped hemispherical shells with precisely manufactured dimple imperfections of Lee et al. [27].

on the level of imperfection, as can be inferred from Fig. 17(*b*). The pressure, $p_{buckled}$, in the stable buckling state at the corresponding value of $\Delta w_{pole}/t$ can be read off Fig. 17(*a*). Plots of p_{max} and $p_{buckled}$ as a function of the probing force imperfection amplitude are presented in Fig. 18 for the case of prescribed volume change. As already noted, the curve for p_{max}/p_C versus δ/t in Fig. 18 is essentially identical to that in Fig. 17 for prescribed pressure, except that for δ/t greater than about 0.7–0.8, depending on R/t, there is no pressure peak under prescribed volume change, as illustrated for the largest imperfection in Fig. 16(*b*). For δ/t outside the range in which a peak pressure exists, ΔV increases monotonically as buckling progresses. The limit of δ/t at which a peak pressure ceases to exist is indicated by the solid dot in Fig. 18.

The behavior of the spherical shell with either a probe force imperfection or a geometric imperfection revealed in Figs. 17 and 18 is very different from the corresponding behavior of the cylindrical shell under axial compression. For spherical shells subject to *prescribed pressure,* there is no distinction between local and global buckling—the shell undergoes complete collapse when the first peak in the pressure is attained. By contrast, the cylindrical shell under prescribed axial load with either type of imperfection first buckles locally into a stable dimple buckle (zone 2) or gradually develops a local buckle (zone 3). Then at a higher load, the shell undergoes global buckling load and complete collapse. As seen in Fig. 17(*a*), the probing force imperfection mimics the geometric dimple imperfection to some extent but, similar to what was noted for the cylindrical shell under axial compression, it produces more severe buckling pressure reductions than those for the dimple imperfection. For spherical shells with probing force imperfections subject to *prescribed volume change,* the shell snap buckles into a state with a stable dimple buckle when the peak pressure is attained, but the pressure the shell can support is much lower than the peak pressure, as seen in Fig. 18, and never recovers. Even though the buckling is local, it coincides with the maximum pressure the shell can support. Similar behavior occurs for the geometric dimple imperfection under prescribed volume change. The behavior of the cylindrical shell wherein global buckling follows local buckling at a higher load does not occur for the spherical shell even under the most rigid loading conditions. Thus, one conclusion to be drawn from this comparison is that code revisions leading to less conservative knockdowns for cylindrical shells under axial compression will not necessarily carry over to spherical shells under external pressure. A second conclusion is that it appears the only way to achieve less conservative knockdowns for unstiffened spherical shells under external pressure is to reduce the level of imperfection. The 1969 recommendation in NASA SP-8032 [29] of a knockdown factor somewhat below $\kappa = 0.2$ independent of R/t for pressure-loaded full spherical shells and hemi-spherical shells clamped at the equator is consistent with the existence of dimple imperfections with amplitudes on the order of a shell thickness or more, as seen in Fig. 17. If less conservative knockdown factors are desired, the shells will have to be manufactured with imperfection amplitudes below one shell thickness.

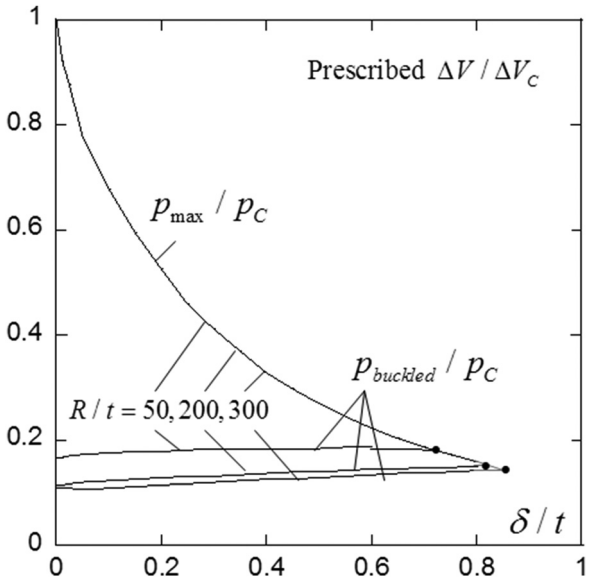

Fig. 18 The maximum pressure prior to buckling, p_{max}, and the pressure in the stable dimple buckled state, $p_{buckled}$, as a function of the probing force imperfection amplitude, δ/t ($= w^0_{pole}/t$) for prescribed volume change. These results have been computed with $\nu = 0.3$. The curve for p_{max} is essentially independent of R/t. Curves for three values of R/t are shown for the pressure in the buckled state. The solid dot indicates the largest value of the imperfection for which snap buckling occurs under prescribed volume change for the specific value of R/t.

6 Conclusions and Potential Lessons Related to Establishing Knockdown Factors

The major findings from this study and their implications for estimating buckling knockdowns of imperfection-sensitive shell structures are enumerated below. The conclusions are based on results obtained in the present paper and in the recent research of others cited above, e.g., see Refs. [3] and [9], for cylindrical shells under axial compression and spherical shells under external pressure, but the insights are likely to be relevant to other shell/loading combinations.

(i) The buckling behavior of a cylindrical shell under axial compression with a probing force imperfection is similar in many respects to the behavior of the shell with a geometric dimple imperfection. For sufficiently small imperfections, local and global buckling occur simultaneously and the roles of the two types of imperfections are similar. For larger imperfections, local buckling occurs first as the load is increased followed by global buckling at a higher load. The global buckling load is relatively independent of the imperfection amplitude and nearly the same for the two types of imperfection. The local buckling load predicted for a probing force imperfection can be appreciably lower than that for a geometric dimple imperfection raising doubts that the probing force can serve as a surrogate imperfection for the geometric dimple imperfection.

(ii) The global buckling load of the cylindrical shell under axial compression is sensitive to the end conditions. For shells that are clamped to rigid end-plates, the global buckling load is significantly lower if one end of the shell can undergo overall rotation relative to the other as opposed to conditions which constrain overall end rotation. Otherwise, the global buckling loads for prescribed axial load and prescribed end shortening are nearly the same, although the global post-buckling behavior of the two cases can be dramatically different. The fact that end-rotation constraint has a relatively small effect on local buckling but a large effect on global buckling is due to the fact that the latter occurs at significantly larger buckling deflections. Apart from the consideration of overall end rotation, this paper has not examined the effect of weak boundary support on reducing buckling loads, which has been addressed by Calladine [30].

(iii) Figure 14 provides the imperfection sensitivity of axial buckling for cylindrical shells with dimple imperfections and draws a comparison with Koiter's worse case imperfection-sensitivity result for an axisymmetric sinusoidal imperfection covering the entire shell. We believe these results span the range of knockdowns that can be expected for unstiffened cylindrical shells as dependent on imperfection amplitude. The results for the first buckling load encountered in the loading history in Fig. 14 are nearly independent of R/t, L/R and

the four sets of end conditions considered in this paper. Given their relevance, more effort is necessary to fully characterize the effects of dimple imperfections and to gain better understanding of when interaction between dimple imperfections becomes important.

(iv) The use of a probing force in an experimental setting to nondestructively explore the stability of an imperfect cylindrical shell under axial compression has been demonstrated. For this purpose, the probe force is not regarded as an imperfection but rather as a tool to probe the shell's stability landscape. A shell subject to prescribed end shortening was evaluated first subject to no overall end rotation. Then, the same shell was evaluated subject to unconstrained overall end rotation, illustrating that unconstrained end rotation lowers the loads relevant to stability. More work is necessary to develop the technique to the point where it can be used as a nondestructive method to measure the buckling load.

(v) The nonlinear buckling behavior of spherical shells under external pressure differs in several important respects from that of cylindrical shells under axial compression—so much so that the common practice of past decades in which the knockdown factor for the cylindrical shell is applied to the spherical shell will be difficult to justify if less conservative factors emerge for the cylindrical shell. Whether the imperfection is a probing force or a geometric dimple, the spherical shell undergoes catastrophic collapse at the first buckling pressure if loaded by prescribed pressure. Under prescribed volume change, the spherical shell snaps to a stable dimple buckle for both types of imperfections. The pressure the buckled shell can support is greatly reduced and never recovers. For the spherical shell under external pressure, the initial buckling pressure is the maximum pressure the shell can support. As in the case of the cylindrical shell, the probing force imperfection gives rise to lower buckling loads than the geometric dimple, and the results in this paper undercut the idea that the probing force imperfection can be taken as a surrogate for a geometric dimple imperfection. As emphasized in Sec. 5, the primary prospect for arriving at less conservative knockdowns for unstiffened spherical shells under external pressure is to ensure the level of imperfection is reduced.

We close this paper by reasserting a view held by many that the type of imperfection invoked to compute buckling knockdowns of imperfection-sensitive structures should be as close as possible to the actual imperfection. This will often require measuring and modeling imperfections associated with a particular manufacturing process and, as many have pointed out, this task can be problematic for structures in the design stage. The computational analysis required in this process may be extensive if less conservative knockdowns are sought, but for sophisticated shell structures such as those employed in the aerospace industry the process is certainly well worth undertaking. Industries where there is less willingness to make the investment to characterize and limit imperfections and to carry out more extensive computations will most likely have to live with more conservative knockdowns. Finally, we have to record that we are somewhat skeptical of the argument that adopting a probing force imperfection as a surrogate imperfection significantly reduces the computational costs of establishing buckling knockdowns, both because this type of imperfection may not be sufficiently realistic, as has been noted, and because analyzing more realistic types of imperfections may not be as daunting a task as is sometimes portrayed.

Acknowledgment

E.V. and S.M.R. acknowledge their involvement in a project directed at new methods for analyzing shell buckling headed by T. M. Schneider at EPFL. E.V. has been supported by this project. This work was also supported by the National Science Foundation through the Harvard Materials Research Science and Engineering Center (DMR-1420570). The authors would also like to thank E. Lozano for extensive comments on the research.

References

[1] Elishakoff, I., 2014, *Resolution of the Twentieth Century Conundrum in Elastic Stability*, World Scientific Publishing, Singapore.
[2] NASA, 1965, "Buckling of Thin-Walled Circular Cylinders," NASA Space Vehicle Design Criteria, National Aeronautics and Space Administration, Washington, DC, Technical Report No. NASA SP-8007.
[3] Rotter, J. M., 2011, "Shell Buckling Design and Assessment and the LBA-MNA Methodology," Stahlbau, **89**(11), pp. 791–803.
[4] Rotter, J. M., 2017, "Challenges and Their Resolution in Both Philosophy and Process to Exploit Advanced Computation in Shell Structure Design," 11th International Conference on Shell Structures Theory and Applications (SSTA 2017), Gdansk, Poland, Oct. 11–13, pp. 2–15.
[5] Hühne, C., Rolfes, R., Breitbach, E., and Teßmer, J., 2008, "Robust Design of Composite Cylinder Shells Under Axial Compression—Simulation and Validation," Thin-Walled Struct., **46**(7–9), pp. 947–962.
[6] Wagner, H. N. R., Hühne, C., Niemann, S., and Khakimova, R., 2017, "Robust Design of Axially Loaded Cylindrical Shells—Simulation and Validation," Thin-Walled Struct., **115**, pp. 154–162.
[7] Krasovsky, V., Marchenko, V., and Schmidt, R., 2011, "Deformation and Buckling of Axially Compressed Cylindrical Shells With Local Loads in Numerical Simulation and Experiments," Thin-Walled Struct., **49**(5), pp. 576–580.
[8] Wagner, H. N. R., Hühne, C., and Niemann, S., 2018, "Robust Knockdown Factors for the Design of Spherical Shells Under External Pressure: Development and Validation," Int. J. Mech. Sci., **141**, pp. 58–77.
[9] Hilburger, M., 2012, "Developing the Next Generation Shell Buckling Design Factors and Technologies," AIAA Paper No. 2012-1686.
[10] Haynie, W., Hilburger, M., Bogge, M., Maspoli, M., and Kriegesmann, B., 2012, "Validation of Lower-Bound Estimates for Compression-Loaded Cylindrical Shells," AIAA Paper No. 2012-1689.
[11] Kriegesmann, B., Hilburger, M., and Rolfes, R., 2012, "The Effects of Geometric and Loading Imperfections on the Response and Lower-Bound Buckling Load of a Compression-Loaded Cylindrical Shell," AIAA Paper No. 2012-1864.
[12] Wang, B., Hao, P., Li, G., Fang, Y., Wang, X., and Zhang, X., 2013, "Determination of Realistic Worst Imperfection for Cylindrical Shells Using Surrogate Model," Struct. Multidiscip. Optim., **48**(4), pp. 777–794.
[13] Hao, P., Wang, B., Tian, K., Du, K., and Zhang, X., 2015, "Influence of Imperfection Distributions for Cylindrical Stiffened Shells With Weld Lands," Thin-Walled Struct., **93**, pp. 177–187.
[14] Evkin, A. Y., and Lykhachova, O. V., 2018, "Design Buckling Pressure for Thin Spherical Shells: Developments and Validation," (submitted).
[15] Koiter, W. T., 1945, "de Stabiliteit van het Elastich Evenwicht," Ph.D. thesis, Delft University of Technology, Delft, The Netherlands.
[16] Koiter, W. T., 1963, "The Effect of Axisymmetric Imperfections on the Buckling of Cylindrical Shells Under Axial Compression," Proc. K. Ned. Akad. Wet., **B66**(5), pp. 265–279.
[17] Árbocz, J., 1982, "The Imperfection Data Bank, a Means to Obtain Realistic Buckling Loads," *Buckling of Shells—A State-of-the-Art Colloquium*, E. Ramm, ed., Springer Verlag, Berlin, pp. 535–567.
[18] Berry, P. A., and Rotter, J. M., 1995, "Partial Axisymmetric Imperfections and Their Effect on the Buckling Strength of Axially Compressed Cylinders," Imperfections I Metal Silos Workshop, Lyon, France, Apr. 19, pp. 35–47.
[19] Wullschleger, L., 2006, "Numerical Investigation of the Buckling Behaviour of Axially Compressed Circular Cylinders Having Parametric Initial Dimple Imperfections," Doctoral thesis, ETH, Zürich, Switzerland.
[20] ABAQUS, 2017, "Software Package, ver. 6.14.4 ed.," Abaqus/Standard, SIMULA, Providence, RI.
[21] Riks, E., 1979, "An Incremental Approach to the Solution of Snapping and Buckling Problems," Int. J. Solids Struct., **15**(7), pp. 529–551.
[22] Virot, E., Kreilos, T., Schneider, T. M., and Rubinstein, S. M., 2017, "Stability Landscape of Shell Buckling," Phys. Rev. Lett., **119**(22), p. 224101.
[23] Hutchinson, J. W., Tennyson, R. C., and Muggeridge, D. B., 1971, "Effect of Local Axisymmetric Imperfections on the Buckling Behavior of a Circular Cylindrical Shell Under Axial Compression," AIAA J., **9**(1), pp. 48–52.
[24] Amazigo, J. C., and Budiansky, B., 1972, "Asymptotic Formulas for the Buckling Stresses of Axially Compressed Cylinders With Localized or Random Axisymmetric Imperfections," ASME J. Appl. Mech, **39**(1), pp. 179–184.
[25] Budiansky, B., and Hutchinson, J. W., 1972, "Buckling of Circular Cylindrical Shells under Axial Compression," *Contributions to the Theory of Aircraft Structures*, Delft University Press, Delft, The Netherlands, pp. 239–259.
[26] Hutchinson, J. W., 2016, "Buckling of Spherical Shells Revisited," Proc. R. Soc. A, **472**(2195), p. 20160577.
[27] Lee, A., Marthelot, J., Jimenez, F. L., Hutchinson, J. W., and Reis, P. M., 2016, "The Geometric Role of Precisely Engineered Imperfections on the Critical Buckling Load of Spherical Elastic Shells," ASME J. Appl. Mech., **83**(11), p. 111005.
[28] Hutchinson, J. W., and Thompson, J. M. T., 2017, "Nonlinear Buckling Interaction for Spherical Shells Subject to Pressure and Probing Forces," ASME J. Appl. Mech., **84**(6), p. 061001.
[29] NASA, 1969, "Buckling of Thin-Walled Doubly Curved Shells," NASA Space Vehicle Design Criteria, National Aeronautics and Space Administration, Washington, DC, Technical Report No. NASA SP-8032.
[30] Calladine, C. R., 2018, "Shell Buckling, Without 'Imperfections'," Adv. Struct. Eng. (in press).